

Controlled Au–Polymer Nanostructures for Multiphoton Imaging, Prodrug Delivery, and Chemo–Photothermal Therapy Platforms

Chih-Chia Huang^{*,†} and Tzu-Ming Liu[‡]

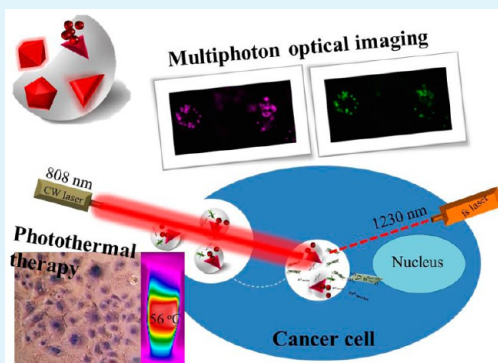
[†]Department of Photonics, Center for Micro/Nano Science and Technology, and Advanced Optoelectronic Technology Center, National Cheng Kung University, 701 Tainan, Taiwan

[‡]Institute of Biomedical Engineering & Molecular Imaging Center, National Taiwan University, Taipei 106, Taiwan

S Supporting Information

ABSTRACT: We have successfully introduced a proton-induced controlled reaction of HAuCl₄ and poly(styrene-*alt*-maleic acid) (PSMA) sodium salt to prepare triangular and multicore Au@polymer nanoparticles (NPs). The interparticle interactions in the core gave rise to an absorption band at the near-infrared wavelength. The near-infrared optical properties of the resulting Au–polymer nanostructures are highly stable in a physiological environment, which offered strong photo-to-thermal conversion by a moderate continuous-wave 808 nm laser and exhibited multiphoton fluorescence for imaging using a 1230 nm light excitation (femtosecond laser). Exposure of the carboxylate groups at the polymer shell made the surface structure of the Au multicore @polymer NPs directly conjugate Pt(II)-/Pt(IV)-based drugs, which possessed the elimination of the immediate toxicity over the short time and resulted in an anticancer effect after 3 days. A synergistic effect of the chemo–photothermal therapy showed a moderate hyperthermia assistance (<1 W/cm²) and better anticancer performance over time compared with the individual treatments. We demonstrated that such PSMA-based methodology not only enables a broad range of chemical material synthesis in the kinetic control to form Au nano-octahedrons and nanotriangles using Br⁻/I⁻ ions additives but also could be extended to form Au/Fe₃O₄@polymer nanocomposites via proton-assisted PSMA self-assembly.

KEYWORDS: Au nanoparticles, shape control, core–shell, multiphoton imaging, prodrug delivery, and chemo–photothermal therapy



1. INTRODUCTION

Since the new concept of specific imaging-guided therapeutic treatment was introduced, various nanomaterials have been developed as smart vehicles for drug delivery or novel theranostic applications.^{1–3} Nanocarrier systems establish different biodistributions of nanomedicines to avoid clearance by the reticuloendothelial system, to permeate through the leaky vessels associated with tumor tissues, and to bind onto tumor microenvironments with functionalized surfaces.^{4–7} For example, Pt-based nanocarriers have shown an efficient anticancer effect in targeting malignant cells.^{5–9} The Pt(IV) nanoprodrug resulted in fewer side effects compared with clinical Pt–complex drugs.^{5–7} Among the developed nanocarriers, gold (Au) nanomaterials have attracted extensive interest because of their relatively inert, biocompatible, and unique optical characteristics. The corresponding surface plasmon resonance (SPR) wavelength can be systematically manipulated from the visible to the near-infrared (NIR) region by changing the geometry of the Au nanomaterials.^{10–13} This tuning of the SPR peak wavelength to the biological transparency window (NIR region) enabled deep tissue optical detection¹⁴ and photothermal therapy.^{15–17} The NIR-laser-excited multiphoton luminescence of the Au/Ag nanoparticles

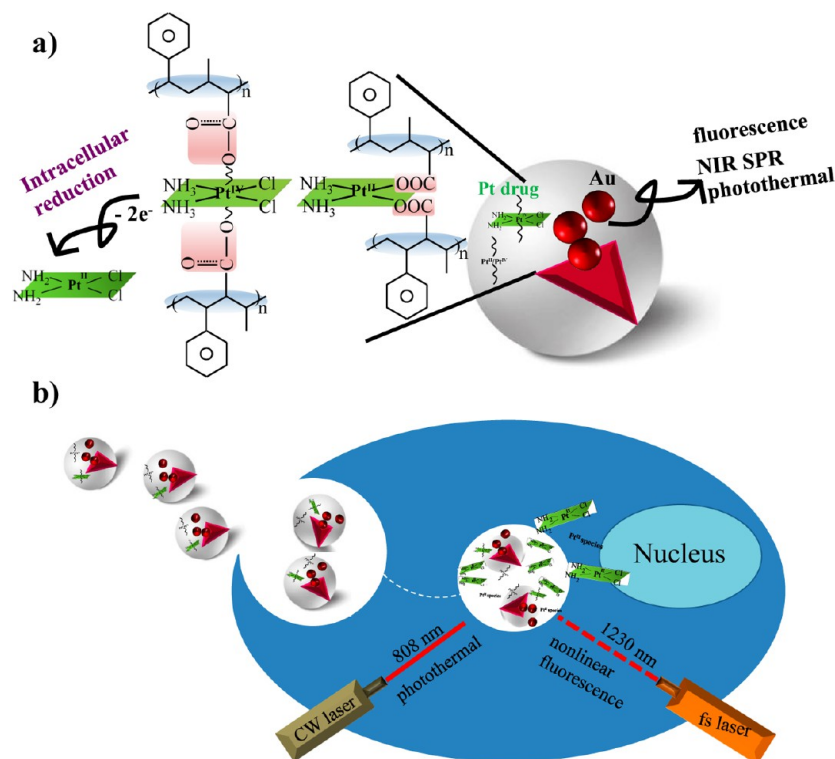
(NPs) was significantly stronger than that of the cellular autofluorescence.^{11–14}

To date, significant efforts have been made to prepare Au NPs with elegant structures, but there remain the most challenging problems of the limited methodology to achieve a tuning of the SPR band to the NIR wavelength for biomedical applications.¹⁸ For example, multiple-step synthesis techniques have been developed, e.g., a seed-mediated process with cationic surfactants for anisotropic Au growth¹⁹ and the galvanic corrosion of an Ag nanotemplate to generate AuAg hollow cage NPs.¹³ The surface engineering of the Au nanocrystals on silica nanospheres, such as Au@SiO₂,²⁰ SiO₂@Au,²¹ SiO₂@Fe₃O₄/Au,²² and NaYF₄@SiO₂@Au nanocomposites,²³ has provided another approach for the synthesis of the desired photofunctional nanostructures. To simplify the synthesis of the NIR-active Au NPs, specific strategies have been adopted, such as structure resonances or interparticle plasmonic coupling.^{22–26} However, these multiple-step reactions inevitably increase the complexity of particle production. Additional postsynthesis procedures have not improved

Received: August 3, 2015

Accepted: October 26, 2015

Published: October 26, 2015

Scheme 1. Multicore Au@polymer NPs^{a,b}

^aIntegrating the Pt(IV) prodrug delivery with NIR-excited photothermal and nonlinear fluorescence. ^bExhibiting simultaneously multifunctional capability of photothermal–chemotherapy and imaging applications to cancerous cell.

chemical waste and toxic surfactants. The Au-based NPs that required a laser power dose of photothermal therapy^{15–17,21–23} over 1 W/cm² have resisted the translation from the laboratory to clinical trials because of the potential risk of burn scars.

In this study, we developed a proton-assisted synthesis strategy based on one-pot approach using poly(styrene-*alt*-maleic acid) sodium salt (PSMA) polymer self-assembly to prepare polymer-encapsulated plasmonic triangular and multicore Au NPs. The multicore Au NPs embedded within the polymer nanostructures exhibited a SPR band in the NIR region, thereby performing an efficient photo-to-thermal conversion with a moderate laser irradiation below 1 W/cm². Because of the interparticle contact interaction in the cluster form, the thermal transformation feature might be improved between each metallic Au NP. The enhancement of the NIR-excited nonlinear optical (NLO) signals was utilized for the fluorescent imaging of the cancer cells that took up the particles. In addition, the carboxylate group of the PSMA polymer assembled onto the Au NPs, which provided additional benefits for the nanocarrier stability in the physiological environment and the direct conjugation of the Pt(II)-/Pt(IV)-based drugs to form the polymer–metal complex (Scheme 1a). The release of the Pt species relied on the intracellular environments but was independent of the light excitation. The IC₅₀ value of this Pt-mediated feature resembled that of the Pt(IV) prodrug. Our previous studies have revealed that the PSMA polymer could absorb different organic drugs²⁷ and could execute targeted photodynamic therapy.²⁸ The present study presented a new contribution for the visualization and therapeutic platform using the Au multicore@PSMA polymer when the biophotonics-bearing NIR laser technology was integrated, as shown in Scheme 1b.

Several advantages are achieved using this technique: (i) 1230 nm light (femtosecond laser) assisted NLO imaging-guided therapeutic ability, (ii) moderate photothermal therapy induced by a continuous-wave (CW) 808 nm laser, (iii) a safe pro-drug delivery system, and (iv) a synergistic effect of the chemo–photothermal therapy.

The fabrication of the polymer–inorganic nanocomposites has attracted great attention for the past decade, especially in optical signal enhancement^{29–31} as well as biomedical applications.^{32,33} Current major fabrication strategies focused on the developments of the interface reaction methodology, such as in situ polymerization of monomers,³⁴ hydrophilic and hydrophobic adsorption,³⁵ and emulsion-based methods,^{32,36,37} for the preparation of metallic nanoparticles embedded in a polymer matrix. Despite the fact that after syntheses of Au/polymer nanocomposites have been well-established, one-pot syntheses of shape-controlled Au nanoparticles@polymer remain a greater challenge. Herein, we demonstrated the proton-controlled synthesis of plasmonic triangular and multicore Au NPs. The coreaction of PSMA and HAuCl₄ solution with Br[−] and I[−] ions could change the reaction kinetics, leading to formation of Au nanotriangles and nano-octahedrons, respectively. Finally, using this proton-assisted PSMA self-assembly strategy, we were able to form magnetic and optical polymer composites consisting of Au multicores and Fe₄O₄ nanoparticles and PSMA polymer nanoshells.

2. EXPERIMENTAL METHODS

2.1. Materials. Poly(styrene-*alt*-maleic acid) sodium salt, 13 wt % solution in water (PSMA, $M_w = 350\,000$) (Sigma-Aldrich), hydrogen tetrachloroaurate(III) trihydrate (HAuCl₄, 99.99%) (Alfa Aesar) and

cis-diamminedichloro-platinum(II) (Pt(NH₃)₂Cl₂, 99.9+%, Aldrich) were purchased and used without purification.

2.2. Preparation of the Au Multicore@Polymer Nanoparticles. HAuCl₄ solution (1 mL, 5 mM) was mixed with 10 mL of a PSMA solution (6 mg/mL) with stirring. Subsequently, 18 μ L of 2 M HCl was added to the solution, which was then immediately transferred to a 23 mL Teflon-lined stainless-steel autoclave and heated at 200 °C. After different reaction times (1–13 h), the as-synthesized product was purified by centrifugation (6000 rpm for 8 min) and washed with distilled deionized water. Large particles were removed by centrifugation at 500 rpm for 2 min, and the supernatant was retained.

2.3. Preparation of the Halides-Induced Synthesis of Anisotropic Au Nanocrystals. HAuCl₄ solution (1 mL, 5 mM) was prereacted with desired volumes of 24 mg/mL sodium halides (NaCl, NaBr, and NaI) for 1 h. The mixture solution was then reacted with 10 mL of a PSMA solution (6 mg/mL) with stirring and then transferred to a 23 mL Teflon-lined stainless-steel autoclave and heated at 200 °C. After 13 h of reaction time, the as-synthesized product was purified by centrifugation (10 000 rpm for 8 min) and washed with distilled deionized water.

2.4. Preparation of the Au/CTA⁺-Coated Fe₃O₄@Polymer NPs. CTA⁺-coated Fe₃O₄ NPs were prepared according to our previous thermal decomposition method followed by a ligand-exchange process with the CTAB surfactants. To prepare Au/CTA⁺-coated Fe₃O₄@polymer nanoparticles, 1 mL of a HAuCl₄ solution (5 mM) was mixed with 10 mL of a PSMA solution (6 mg/mL), 18 μ L HCl (2 M), and the CTA⁺-coated Fe₃O₄ NPs (200 ppm [Fe]) under vigorous stirring. The mixed solution was then transferred to a 23 mL Teflon-lined stainless-steel autoclave and heated at 200 °C for 13 h. After reacting, the as-synthesized magnetic product was purified by centrifugation (4000 rpm for 8 min) and washed with distilled deionized water. The precipitated materials were removed by centrifugation at 500 rpm for 2 min, and the supernatant solution was retained. We collected the magnetic Au/CTA⁺-coated Fe₃O₄@polymer NPs from the supernatant solution after applying a magnet.

2.5. Conjugation of Cisplatin with the PSMA Polymer on the Au Multicore. The conjugation of the Au multicore@polymer with cisplatin to form the Pt–polymer complex at the Au multicore was carried out as follows. The Au multicore@polymer NPs (0.4 mL, 600 ppm [Au]) were mixed with 0.2 mL of cisplatin (0.019 M) followed by a reaction with 0.125 mL of H₂O₂ (34.5%). After 2 h of sonication treatment, the resultant nanoparticle was purified by a centrifuging/redispersion process followed by centrifugation at 6000 rpm to remove the excess Pt-based and H₂O₂ reagents and then redispersed in a dilute water solution.

2.6. In Vitro Release Studies of the Pt Drug from the Pt-Medicated Au Multicore@Polymer NPs. Esterase (9.6 μ L) (28.1 μ g/mL) was reacted with 800 μ L of the Pt-mediated Au multicore@polymer NPs (600 ppm [Au]) at 37 °C. After 0.5, 1, 3, 6, 12, 24, and 48 h, the supernatants were collected and analyzed via an ICP-AES measurement. Parallel experiments with the release of the Pt drugs from the Pt-mediated Au multicore@polymer NPs in a PBS solution (dark condition at 37 °C) and the Pt-mediated Au multicore@polymer NPs in a water solution (under 808 nm light excitation) were carried out by an ICP-AES measurement.

2.7. Temperature Examination under 808 nm Laser Irradiation. The temperature elevation of the Au multicore@polymer NPs was measured by placing the material solutions (350 ppm [Au]) in 96-well plates and irradiating them using an 808 nm CW diode laser. A thermocouple was immersed in the material solution to determine the temperature. The CW laser had a power density of 1.5 W/cm². For the infrared thermographic map examinations, 1 mL of the Au multicore@polymer NPs solution (350 ppm) in a 1.5 mL centrifuge tube was reacted with an 808 nm light at power densities of 0.82 and 0.4 W/cm². The thermal images of these solutions were monitored from 0 to 10 min using a thermographic camera (Fluke/FLK-TI32 9HZ).

2.8. Photothermal Therapy of the A549 Cancer Cells. The A549 cancer cells were cultured in 96-well plates with DMEM and

maintained in an incubator under a 5% CO₂ atmosphere at 37 °C. Each well contained 8000 cells for a culture time of 24 h. The 250 ppm [Au] amounts of Au multicore@polymer NPs and the Pt-mediated Au multicore@polymer NPs were individually added to the cells and incubated for 4 h at 37 °C. To remove the unbound nanoparticles, the wells were rinsed with PBS buffer, and then fresh DMEM media was added to each well. The photothermal killing of the cancer cells was carried out using a CW diode laser with a wavelength of 808 nm (0.82 W/cm²) for 10 min. After laser irradiation, another 24 h incubation was carried out. We utilized MTT assays to examine the cell viability.³⁸ Briefly, the original culture medium was removed and replaced with 100 μ L of new culture medium containing 10% MTT reagent. To yield formazan dye, the cells were then incubated for 4 h at 37 °C. The culture medium in each well was then removed. Dimethyl sulfoxide (DMSO, 200 μ L) was added in each well for an additional 10 min of incubation. Finally, the resulting formazan in each well was transferred to an ELISA plate after centrifugation. Quantification analysis was carried out using a scanning multiwell ELISA reader at 485 nm (SpectraMax M2^e, Molecular Devices, USA) to determine cell viability.

2.9. Nonlinear Optical Microscopic Imaging. To evaluate the multiphoton fluorescence contrast, the Pt-loaded Au multicore@polymer NP treated cells were studied. The laser wavelength operates at approximately 1230 nm, which falls in the NIR penetration window (1200–1300 nm) of most biological tissues. The laser beam was XY-scanned by a scanning unit (FV300, Olympus) cascaded with an inverted microscope (IX71, Olympus). The laser beam transmitted by a multiphoton dichroic beam splitter (edged at 665 nm) and was focused using a water immersion objective (NA = 1.2, 60 \times , Olympus). The generated second-harmonic generation (SHG) and third-harmonic generation (THG) were epi-collected by the same objective. The CCD of spectrometer is silicon-based and would not have significant photoresponses for wavelengths longer than 1100 nm. We used a multiphoton dichroic beam splitter edged at 865 nm and a KG5 color glass short-pass filter right before the entrance of spectrometer. These optics in the system will further reduce the 1230 nm light back-reflected into the spectrometer.^{39,40}

To image the live cells after treatment with the particles for 2 and 24 h, a microincubator on a microscope was used at a temperature of 37 °C in an environment that was 5% CO₂/95% air. The temperature of the thermostat (LAUDA Ecoline Staredition RE 204) was set to 50 °C to achieve 37 °C at the distal ends of the objective, but the vapor reaching the microincubator through the duct maintained the microincubator at approximately 37 °C. The gas controller (OkO Lab) continuously supplied 5% CO₂ and maintained the outlet absolute pressure at 1 atm. The water-immersion objective with 1.2 NA was heated by a dual-temperature controller (TC-144, WARNER instrument), making the temperature at the bottom of the dish that contacted the objective approximately 37 °C. The SHG and THG signals were reflected and then separated by another dichroic beam splitter edged at 490 nm; they were detected separately by two other PMTs. The three-signal channels were reconstructed to 512 \times 512 pixels images with computer software at a 2 Hz frame rate.

2.10. Characterization. Transmission electron microscopes (TEMs, JEOL 3010 at 300 kV and JEM-2000EX II at 80 kV) were used to obtain a more accurate estimate of the solid particle size. The absorption spectra of the Au multicore@polymer nanoparticles were measured using a UV–vis spectrophotometer (8452A; Hewlett-Packard Co., Palo Alto, CA). The Au concentration of the Au multicore@polymer nanoparticles solution was quantified by inductively coupled plasma atomic emission spectrometry (ICP-AES, JY138 Spectroanalyzer; Horiba Jobin Yvon, Inc., Edison, NJ). The zeta potential and hydrodynamic diameter of the nanoparticle samples dispersed in an aqueous solution were measured using a Zetasizer analyzer (Malvern, UK). The magnetic nanoparticles were magnetized (*M*–*H* loops) at 300 K with applied fields of up to 40 kOe using a Quantum Design MPMS-7 SQUID magnetometer.

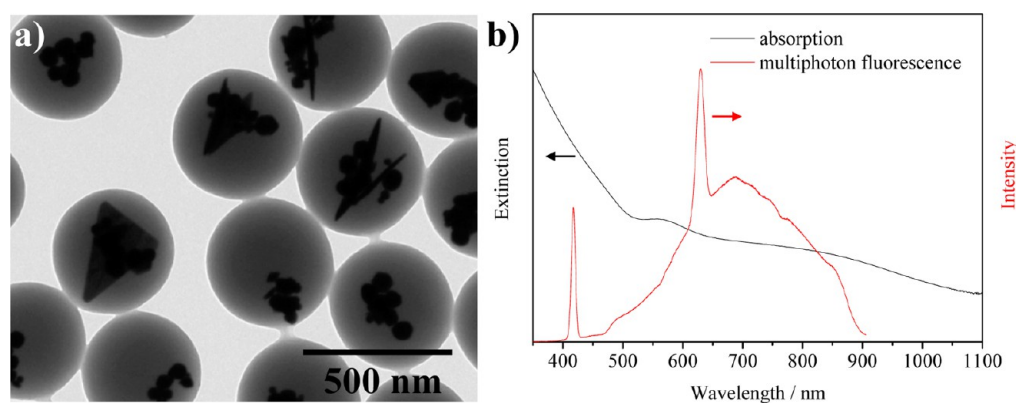


Figure 1. (a) TEM images and (b) UV–visible absorption (black curve) and nonlinear optical responses (red curve) with 100 fs laser excitation at 1230 nm for Au@polymer nanoproducs prepared with 18 μL of HCl (2 M).

3. RESULTS AND DISCUSSION

Our current result shows that a hydrothermal reaction (at 200 $^{\circ}\text{C}$ after 13 h) of 1 mL of HAuCl_4 (5 mM) and 10 mL of poly(styrene-*alt*-maleic acid) sodium salt (PSMA) polymer (6 mg/mL) produced a single-domain Au NP core within a polymer sphere (Au@polymer).²⁷ In this study, we introduced a pH-guided synthesis strategy to engineer the polymer self-assembly and the aggregation of the Au NPs to generate the NIR absorption. Figures 1a and S1a show a TEM image from a reaction of 6–18 μL of HCl solution with HAuCl_4 and the PSMA polymer at 200 $^{\circ}\text{C}$ after a hydrothermal treatment for 13 h. Only three precursors were used. It was observed that the resulting polymer nanospheres could encapsulate 1–6 Au NPs at 6 μL of HCl and 11–20 NPs at 12 μL of HCl. These encapsulated Au NPs became increasingly closer as the amount of HCl was increased to 18 μL . The size of the Au NPs decreased at a low HCl amount. Notably, the formation of the anisotropic nanoaggregates and the triangular Au nanoplates (dark contrast) was obtained and embedded in the polymer spheres (light contrast), leading to the production of the Au multicore and the PSMA shell nanostructures at 18 μL of HCl. Figures 1b (black curve) and S1b show the corresponding absorption spectra of these samples, demonstrating the gradual evolution of the ensemble-averaged SPR band of the Au NPs. Note that with the increase in the HCl the SPR band broadened and the 600–1000 nm NIR absorption increased which might be due to the plasmonic coupling effects among the Au NPs and the anisotropic Au nanostructures.

Surprisingly, we prepared methylene blue (MB)-loaded Au multicore@polymer NPs, and these particles did not exhibit a good SERS signal response at 633 and 785 nm, despite the significant local-electric-field enhancement by the SPR (data not shown). Although the PSMA surface structure helped to trap the MB molecule, the thicker polymer coating layer prevented the MB from approaching the Au surface.²⁷ In contrast, a superior THG at ~ 410 nm, a SHG at ~ 615 nm, and a two-photon fluorescence (TPF) at 650–900 nm were generated on the Au multicore@polymer NPs, as shown in Figure 1b (red curve). All of the NLO signals significantly increased compared with those of the single-domain Au@polymer NPs (13 h sample). The overall luminescence intensity was approximately 20 times (with a 10 s integration time) higher than that of the single-domain Au@polymer NPs (with a 30 s integration time). As the amount of HCl was increased from 0 to 18 μL (Figure S2), the THG, SHG, and TPF

intensities further increased. The manipulation of the plasmonic Au coupling enabled the tuning of the shift of the SPR wavelength to a long wavelength, thereby enhancing the NLO intensity. The redshift of the SPR band toward 800–1000 nm enhanced the efficiency of the NIR-excited TPF.^{41–43}

To characterize the intrinsic absorption feature of Au multicore, the optical scattering interference by polymer-capping shell was cleared by adding 10 mM NaOH solution (Figure S3a). Apparently, the molar extinction coefficient of Au multicore alone solution decreased from ~ 903 to ~ 433 cm^{-1} M^{-1} at 808 nm, whereas NIR absorption band was still retained (Figure S3b). At least half the intensity of NLO signal was sustained after removing the polymer shell on the Au multicore with respect to the decrease of extinction coefficient value (Figure S3c).

To gain a deeper insight into the effects of the acid on the synthesis, time-dependent TEM images (Figure S4a) were acquired to investigate the assembly process. Using 18 μL of HCl at a 1 h reaction time, no formation of the Au nanoproducs occurred. Larger Au particles with polyhedral shapes (triangle, pentagon, and hexagon) and many free polymer NPs appeared at 2 h. Compared with the acid-free synthesis,²⁷ only 1 h was required to achieve the SPR band that required 2 h with the acidic synthesis. This result indicated a change in the formation kinetics of the Au NPs with the addition of the HCl solution. As the reaction was prolonged to more than 6 h, the free polymer particles and the Au@polymer nanocomposites started to fuse together, and the triangular Au nanoplate grew larger. Studies on the synthesis reactions under the acidic condition and with carboxylate groups⁴⁴ have shown that these conditions caused the metallic NPs to grow preferentially along the (111) plane. X-ray photoelectron spectroscopy (XPS) and near-edge X-ray absorption fine structure spectroscopy validated the carboxylate group strongly bonding onto the (111) plane of Au atoms.⁴⁵

The UV–visible spectra (Figure S4b) recorded the continuous evolution of the local LSPR extinction at ~ 810 nm as the reaction time increased. As we expected, the extinction peak shifted to the NIR wavelength when the Au NPs aggregated each other.^{17,23–26} The large triangular Au nanoplates might also contribute to the NIR absorption.

The reduction reaction of the Au^{3+} species to form the Au NPs should occur simultaneously with the oxidation of the carboxylate-rich PSMA polymer. The amphiphilic PSMA polymer was composed of a polycarboxylate/-carboxylic portion and hydrophobic polystyrene, which exhibited

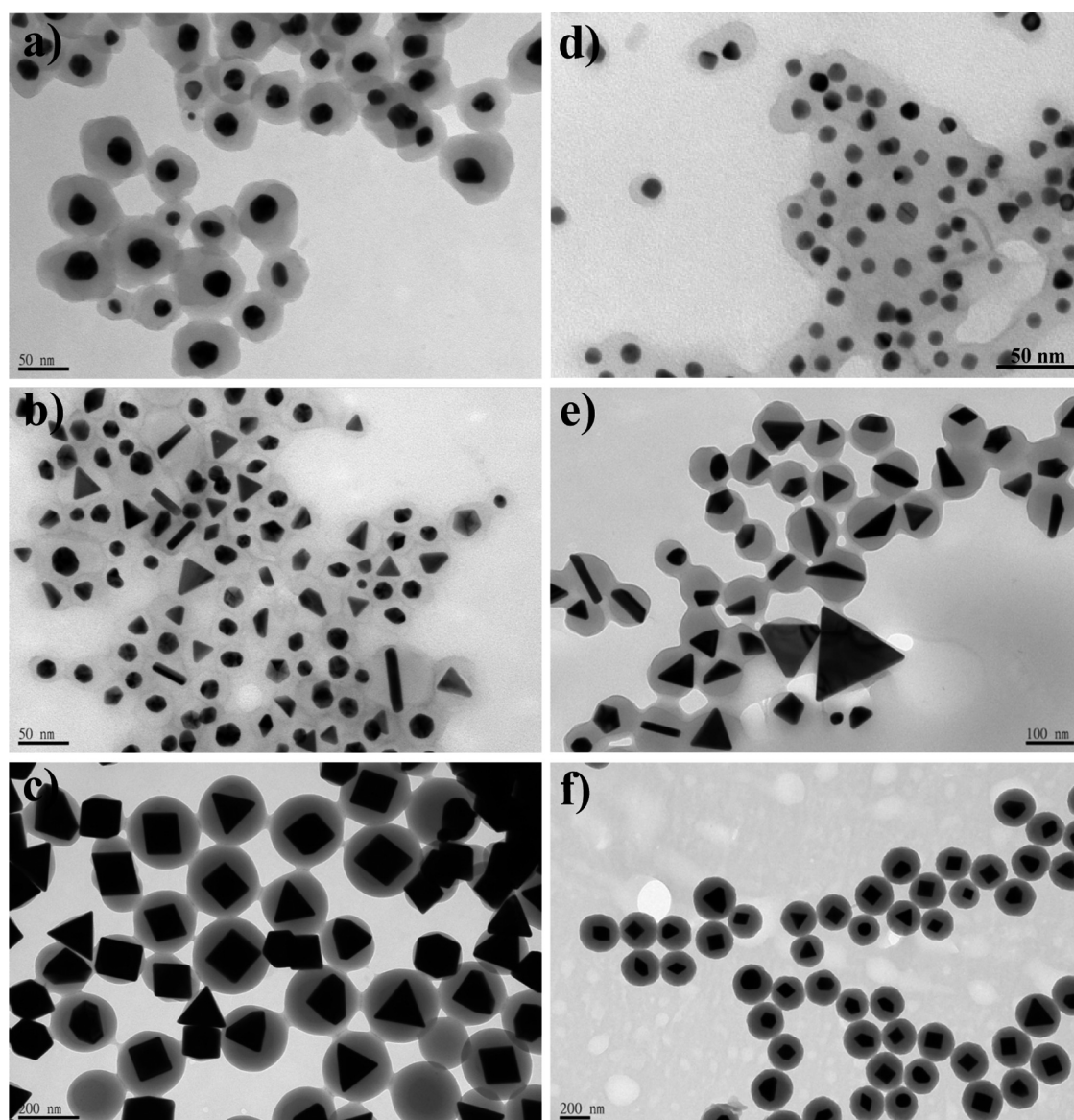


Figure 2. TEM images of the preparation of Au nanocrystals@PSMA polymer via reacting HAuCl_4 and PSMA solution with (a) 75 μL of NaCl (24 mg/mL), (b) 75 μL of NaBr (24 mg/mL), (c) 75 μL of NaI (24 mg/mL), (d) 10 μL of NaI (24 mg/mL), (e) 75 μL of NaBr (24 mg/mL) plus 20 μL of NaI (24 mg/mL), and (f) 75 μL of NaBr (24 mg/mL) plus 40 μL of NaI (24 mg/mL). These hydrothermal reactions were carried out at 200 $^\circ\text{C}$ for 13 h.

chelation, π -stacking, and pH-sensitive behaviors.^{46–49} The low pH and appropriate salt participation were studied, favoring the regular and rigid stacking of the benzene rings into a tubular formation by the 3D association of the PSMA polymer.⁴⁸ In our continued effort to control the Au nanostructures via the molecular interaction of the PSMA polymer self-assembly process, we realized that the addition of a HCl solution gave rise to an internal H bond (protonation) of the PSMA polymer onto the Au NPs, leading to the dispersion of the Au NPs that were densely packed into the polymer capsule. On the basis of the HCl- and time-dependent TEM and UV–visible examinations (Figures 1, S1, and S4), these results indicated that the low pH and hydrogen bond interaction among the Au@polymer NPs played a pivotal role, causing slow growth kinetics for the formation of the Au–polymer nanocomposites. A higher HCl amount enabled the etching of the Au atoms by dissolving the fresh clusters. We suggest that the anisotropic growth to larger and triangular Au NPs would progressively

occur by a dissolution–recrystallization process in addition to the interparticle aggregation with the assistance of the acid.

In a control experiment carried out by reacting at 180 $^\circ\text{C}$ while maintaining the other parameters, the yield of the Au multicore@polymer NPs remained and did not produce triangular-shaped particles (Figure S5). The particle size was estimated as 200–300 nm. Interestingly, these particles possessed a shoulder absorption band at ~ 850 nm, implying the dominant contribution of the interparticle aggregation and the size and aspect ratio of the Au nanoparticles, leading to the promotion of the absorption band at the NIR wavelength.

Inspired by the controlled growth kinetics of Au nanocrystals,^{50,51} we pretreated the HAuCl_4 solution with 75 μL of sodium bromide and sodium iodide for 1 h, leading to replacement of Au–Cl complex to form Au(III)–Br/Cl and Au(III)–I/Cl complexes, respectively. The coordination of Au species with Br^- and I^- ions was likely due to lower reduced potential levels according to a decline trend in the standard

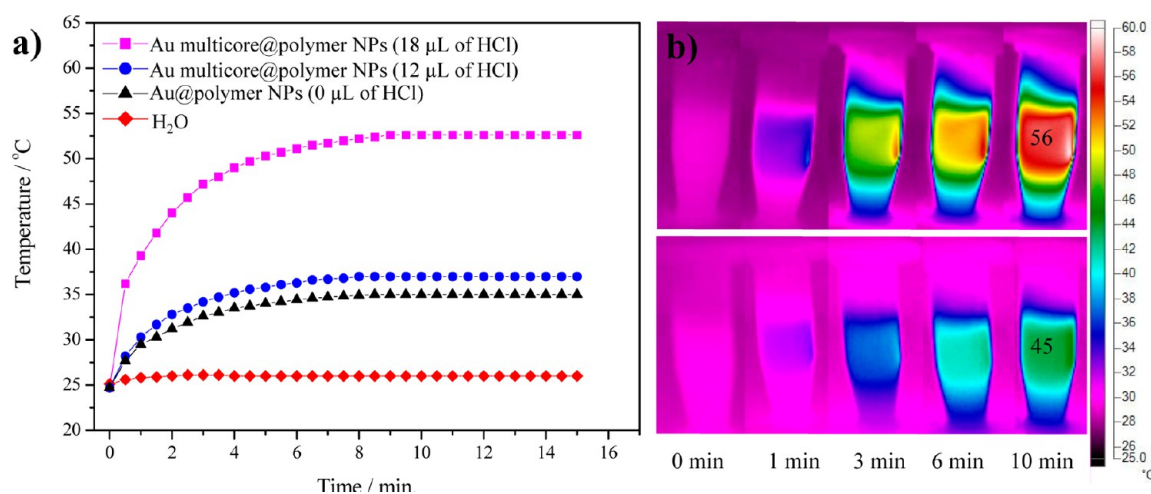


Figure 3. (a) Temperature dependence of the 0.1 mL Au multicore@PSMA NPs, prepared with 0, 12, and 18 μL of HCl and water, as a function of irradiation time. (b) Infrared thermographic maps of the 1 mL Au multicore@polymer NPs (350 ppm) with a dose of 0.82 W/cm^2 (top) and 0.4 W/cm^2 (bottom), captured with a thermographic camera.

compounds: $\text{AuCl}_4^-/\text{Au}$, 0.93 V vs SHE, $\text{AuBr}_4^-/\text{Au}$, 0.854 V vs SHE, and AuI_4^-/Au , 0.56 V vs SHE. The reaction with NaBr additive produced triangle- (~24%) and pentagon-shaped (~9%) Au@polymer nanoparticles (Figure 2b). The average diameter was estimated as ca. 28 nm. Figure 2c shows a TEM image from which was estimated a yield of >65% and an average edge length of ca. 128 nm in the formation of the Au nano-octahedrons within the polymer shell by using NaI-assisted synthesis. An SEM image determined that several nano-octahedrons were isolated from the polymer sheath (Figure S6a). The fabrication of small-sized Au nano-octahedrons@polymer (~8 nm) was obtained by reacting with 10 μL of NaI (Figure 2d). In contrast, by adding 75 μL of NaCl (Figure 2a), the Au–polymer nanostructure was almost the same as that of the acid- and NaCl-free synthesized nanoparticles.²⁷

Because the binding strength of the halides to Au ions follows the order of $\text{I}^- > \text{Br}^- > \text{Cl}^-$ as well as the reduced potential alteration,⁵⁰ we anticipate that the addition of a trace of I^- ions in the HAuCl_4 –NaBr solution system would further slower the reduction potential and decrease the number of the Au nuclei. Growth of the bigger particle size relied on the slow formation kinetics and resulted in the generation of fewer nucleus in this redox system. Apparently, the Au nanotriangles have a 68 nm average edge length with ~72.5% yield rate at 75 μL of NaBr and 20 μL of NaI (Figures 2e and S6b), whereas the structure of Au nanocrystals converted to Au nano-octahedrons@polymer (~80%) had an average octahedral edge length of ca. 94 nm when 40 μL of NaI was coreacted with 75 μL of NaBr solution (Figure 2f). Results (Figure 2) showed octahedral, triangle, and pentagonal structures consisting of {111} planes. We suggest that Br^- and I^- ions not only interfered the redox potential and binding strength of Au complex precursors⁵⁰ for decreasing the nuclei number with slower crystal growth rates but also were primarily absorbed together with PSMA polymer capping on the certain planes in particular inhibits the growth along the <111> direction. However, the true mechanism in the formation of the {111}-enclosed Au nanocrystals is still up for debate, which will be studied further and reported in our next paper to address the possibility of controlling the reduction rate and shape progression.

Compared with the popular Turkevich method^{52,53} based on the thermal reduction of aurate ions (AuCl_4^-) with citrate molecules, the most accessible result was that in which the size of the Au NPs was tuned while preventing the SPR band from shifting to the NIR region. We utilized the polycarboxylated PSMA polymer to react with HAuCl_4^- , giving rise to reproducible yields of different Au–polymer nanostructures and their corresponding visible–NIR SPR bands that depended on the reaction parameters (reaction time and HCl concentrations). We established that the NIR absorption band of the polymer-coated multicore Au NPs was highly stable against aggregation in the PBS solution whereas the citrate-capped Au NPs were not. The halides-induced anisotropic growth of Au nanocrystals@polymer provided an alternative method of being able to control the particle's sizes and shapes. A complete interpretation of the halide-complex and -capping effects is beyond the scope of this paper, which focused on the proton-assisted reaction.

Because of its strong SPR features in the NIR region (Figure 1b, black curve), the photothermal effect of the Au multicore@polymer NPs deserves additional photothermal therapeutic efforts. Exploiting the raised NIR absorption, we excited the Au multicore@polymer NP solution (350 ppm [Au]) with a 808 nm laser (0.82 W/cm^2 intensity) and recorded the water temperature as a function of time (Figure 3a). A remarkable photo-to-thermal conversion occurred only for the product obtained with 18 μL of HCl. The solution temperature rapidly increased to 44 °C after 2 min and increased further to 52 °C at ~7.5 min. By comparing these results with those of other Au–polymer samples and water, we concluded that the strong photothermal conversion resulted from the higher NIR absorption of the NPs. A thermal imaging camera was used to directly monitor the photothermal efficiency of the Au multicore@polymer NPs under the laser irradiation. Figure 3b revealed the continuous temperature increase of the sample solution from 56 to 45 °C as the irradiation time increased (from 0 to 10 min) with intensity levels of 0.82 and 0.4 W/cm^2 , respectively. A moderate laser power density was sufficient for the Au multicore@polymer sample to achieve hyperthermia destruction of tumor cells. This efficient heat conversion might be ascribed to the formation of metallic multi- and nanocores, favoring light absorption due to the interparticle plasmonic

coupling and the good thermal transformation among each of the Au NPs.

The zeta potential measured for the as-prepared Au multicore@polymer NPs was -41 mV, implying that the carboxylate groups were exposed at the surface. We believe that the numerous COO^- functional groups at the surface of the Au multicore@polymer NPs could be used to coordinate the inorganic metal ions. Because the toxicity and side effects of the Pt(IV) compounds are less severe than those of the Pt(II) drug (i.e., cisplatin),^{4–6,54–56} to the conjugation process was added H_2O_2 to oxidize the cisplatin. The XPS analysis determined the existence of Pt ions in the PSMA polymer structure (Figure S7). Similar to the formation of lipoic poly(acrylic acid)-bonded Pt(II) complex on the Au nanoparticles by Lee et al.,⁶ we propose that the carboxylate blocks at PSMA polymer possessed coordinated activity to interact with Pt(II) species as well as the oxidized Pt(IV) ions. Figure 4 shows that the peak

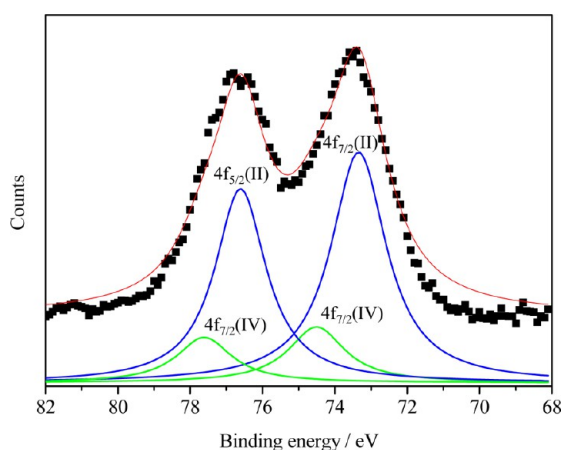


Figure 4. XPS spectra for Pt 4f regions collected from as-prepared Pt-mediated Au multicore@polymer NPs.

deconvolution for Pt 4f binding energies can be split into respective peaks related to Pt (II) and (IV). The Pt 4f binding energies at 76.5 eV ($4f_{5/2}$) and 73.3 eV ($4f_{7/2}$) are close to those of the Pt^{2+} -N complex structure.⁵⁷ The positions of the peaks Pt($4f_{7/2}$) and Pt($4f_{5/2}$) exist at higher binding energy, which were assigned to Pt(IV) species complexed with PSMA polymer. A $[\text{Pt}]/[\text{Au}]$ molar ratio of approximately 0.008 in the Pt-mediated Au multicore@polymer nanocarrier (shortened to Pt-based nanocarrier) was estimated using an ICP-AES measurement. It has been established that the Pt(IV) prodrug exhibited a chemically activated anticancer action when the drug was delivered into the cell because of the reducing intracellular environment, such as glutathione.⁵⁸ In addition to the known intracellular environment, we discovered that the release of the Pt drugs from the Pt-based nanocarrier was enhanced nearly twofold by reacting with an esterase compared with that of the incubation in the PBS solution. This esterase-induced release is possibly due to the degradation of the ester-linking PSMA polymer,²⁷ poly(lactide-co-glycolide) (PLGA) scaffold,⁵⁹ and polyurethanes.⁶⁰ An esterase is a hydrolase enzyme supported by living cells that aids the hydrolysis of the ester bonds into an acid and an alcohol. The degradable property of the PSMA polymer shell readily further aided the toxic drug effect that occurred within the cellular environment. The leaching of the Pt species was inactive (less 15%) because

of lengthy storage in the PBS solution or the heating effect on the NIR light excitation (Figure S8).

Prior to the biological examinations, the optical performance of Au multicore@polymer NPs was further analyzed because the PSMA polymer structure would be damaged by enzymes in a biological environment. Primarily, complete removal of polymer shell on the Au multicore was examined by reacting with the NaOH solution, and the corresponding optical responses were studied. We noted that the optical features of Au multicore@polymer NPs resulted in a decrease of the absorption and fluorescent intensities after completely peeling of polymer shell (Figure S3b,c). The corresponding NLO intensity was strong enough to allow the imaging detection in the NLO microscope. However, the thermal conversion efficiency⁶¹ of the Au multicore@polymer NPs was estimated to be $\sim 14\%$ and could be improved to $\sim 23\%$ after the removal of the polymer shell (Figure S3d). This promotion would be ascribed to a consequence of the decreased light scattering by the surface coating polymer and increase in the Au multicore photon absorption. Our demonstrations presented the applicability of the Au multicore@polymer NPs in NLO imaging and photothermal therapy when the enzymes lysis appeared in biological environment.

The MTT assay was carried out to ascertain the cell viability of the A549 lung cancer cells treated with the Pt-based nanocarrier. As shown in Figure S9, the Pt-based nanocarrier did not have significant toxicity on the cells after a 1 day incubation. The $\text{IC}_{50}[\text{Pt}]$ value was close to 500 ppm $[\text{Au}]$ of the Pt-mediated nanocarrier after an incubation of 3 days. The elimination of the immediate toxicity over the short term resembled the Pt prodrug behavior.^{8,9} The longer incubation time required to observe the anticancer effects was most likely due to the slow conversion of the Pt(IV) prodrug from the polymer backbone to the Pt(II) species^{54,55} and/or the dissociation of Pt(II)/Pt(IV) from the polymer-metal complex in the cellular reduction environment.

Using multiphoton NLO microscopy to image these live cells, we treated live A549 lung cancer cells with the Pt-based nanocarriers and monitored the outcome at two times, 2 and 24 h. After 2 h of incubation (Figure Sa, left), a portion of the particles was taken up by the cells, which was easily confirmed by the SHG (green color) and THG (magenta color) images. The SHG and THG images were superimposed, showing that these local signals originated from the same particles. In contrast, the cells alone did not exhibit significant nonlinear signals even as we increased the excitation power from 1 to 60 mW (Figure S10). That means the loading agent provided strong contrast ability, requiring only 1/60th of the laser power to give enough SHG and THG contrast. After exposing the cells to the Pt-mediated nanocarriers for 24 h, the number of bright dots with strong SHG and THG images increased and appeared to aggregate around the nuclear periphery, showing a margin delineation of the nuclei (Figure Sb, right). It was believed that the Au@polymer NP could reside within the cell body according to the NLO microscopy observations. This suggests that the Pt-mediated nanocarrier accumulated in the endocytic vesicles via an endocytosis pathway, a process that is time-dependent. Consequently, the release of the Pt species in the perinuclear space of the cells might be efficiently transferred into the nuclei and damage the DNA, a subject which requires further studies.

To evaluate the photothermal effect combined with chemotherapy, the experiments for the cell viabilities by the

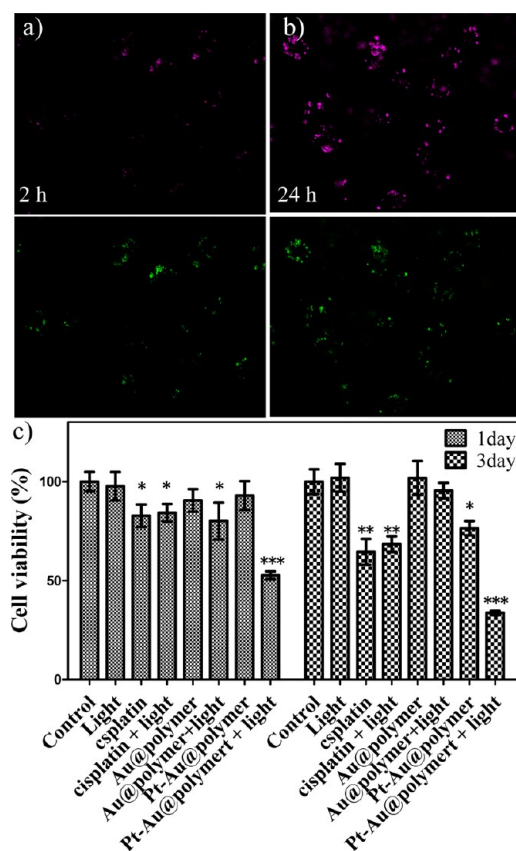


Figure 5. THG microscopy (top) and SHG microscopy (bottom) of the A549 cells treated with the Pt-mediated nanocarrier for (a) 2 h and (b) 24 h, using a 1230 nm laser with 10 mW of power and 10 s of integrated time. (c) MTT assay for the A549 cells incubated with 250 ppm_[Au] of the Pt-mediated nanocarrier for 4 h (with the removal of the excess nanocarrier) followed by exposure to 808 nm light irradiation (0.82 W/cm²) for 10 min. The cells were cultured for another 1 and 3 day(s) before the MTT assay. Cisplatin concentration is 2 μM.

incubation of the cells with the Au multicore@polymer NPs along with the NIR laser and the Pt-mediated nanocarriers with the NIR laser were carried out (Figure 5c). Cells interacted with cisplatin drug alone (2 μM) were inactive with irradiation by 808 nm laser light. After allowing the

interaction among the A549 cells and the nanocomposites for 4 h, the particle-treated cells were washed with the PBS buffer solution and then exposed to a moderate NIR laser treatment at 0.82 W/cm² for 10 min. Subsequently, another 1–3 days of incubation time was carried out. Approximately 48% of cells at 1 day and 66% of cells at 3 days were killed by treatment with the Pt-mediated nanocarriers and 808 nm light. Figure 6a showed that most of the particle-treated plus laser light cells stained with trypan blue showed blue color after 3 days of incubation time. Though long-term culture resulted in good anticancer efficiency, we observed a less color in cellular imaging in control cells (Figure 6b). It is not surprising that serious harm for these cells (up to 63 and 85% of cell death at 1.69 and 2.3 W/cm², respectively) appeared at 1 day when Pt-mediated nanocarriers and higher laser power densities were employed (Figure S10). Possibly, the application of high laser power density may also carry a risk of side effects to human body in the surrounding tissue because of the generation of undesired thermal injury.

As expected, the Pt-mediated nanocarriers alone caused no significant cellular toxicity at 1 day. Nearly ~75% cell viability was obtained after 3 days of incubation time. Conversely, the reduction of the cell viability to 80% occurred after 1 day when the cells were treated with the Au multicore@polymer NPs and moderate NIR light. Because of the elevated temperatures, the generation of heat would immediately cause cell harm. However, these cells favored regeneration after 3 days. Compared with chemotherapy combined with photothermal therapy, the appearance of the lower cytotoxicity by the different control experiments could be explained by the absence of the synergistic effect. In addition, we anticipated that the release of the Pt anticancer drug accumulation within the cells over time might assist the short-term photothermal ablation of the cancerous cells and restrict cancer cell regeneration.

Finally, in principle, the acid-mediated PSMA self-assembly can be applied to develop a new synthesis methodology for the preparation of other novel inorganic–organic nanohybrids. Impressively, we could utilize an electrostatic interaction strategy by the absorption of the negatively charged PSMA polymer to the positively charged CTA⁺-coated Fe₃O₄ NPs, thus enabling in situ self-assembly with the Au NPs. The inset in Figure 7a shows the TEM image of the multicore and triangular-shaped Au NPs multicore and the CTA⁺-coated

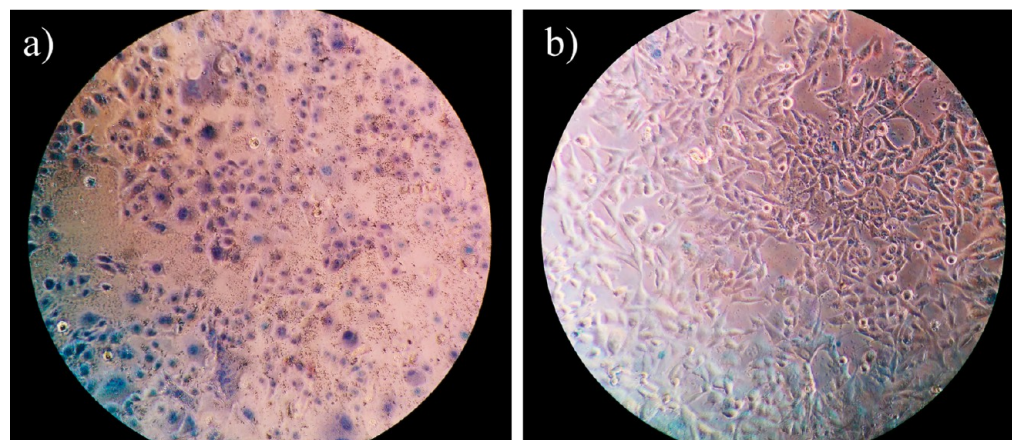


Figure 6. (a) Pt-mediated nanocarrier-treated cells and (b) cells alone after 4 h of culture time (with PBS washing) followed by exposure to 808 nm light irradiation (0.82 W/cm²) for 10 min. These cells were stained with trypan blue after another 3 days of culture time.

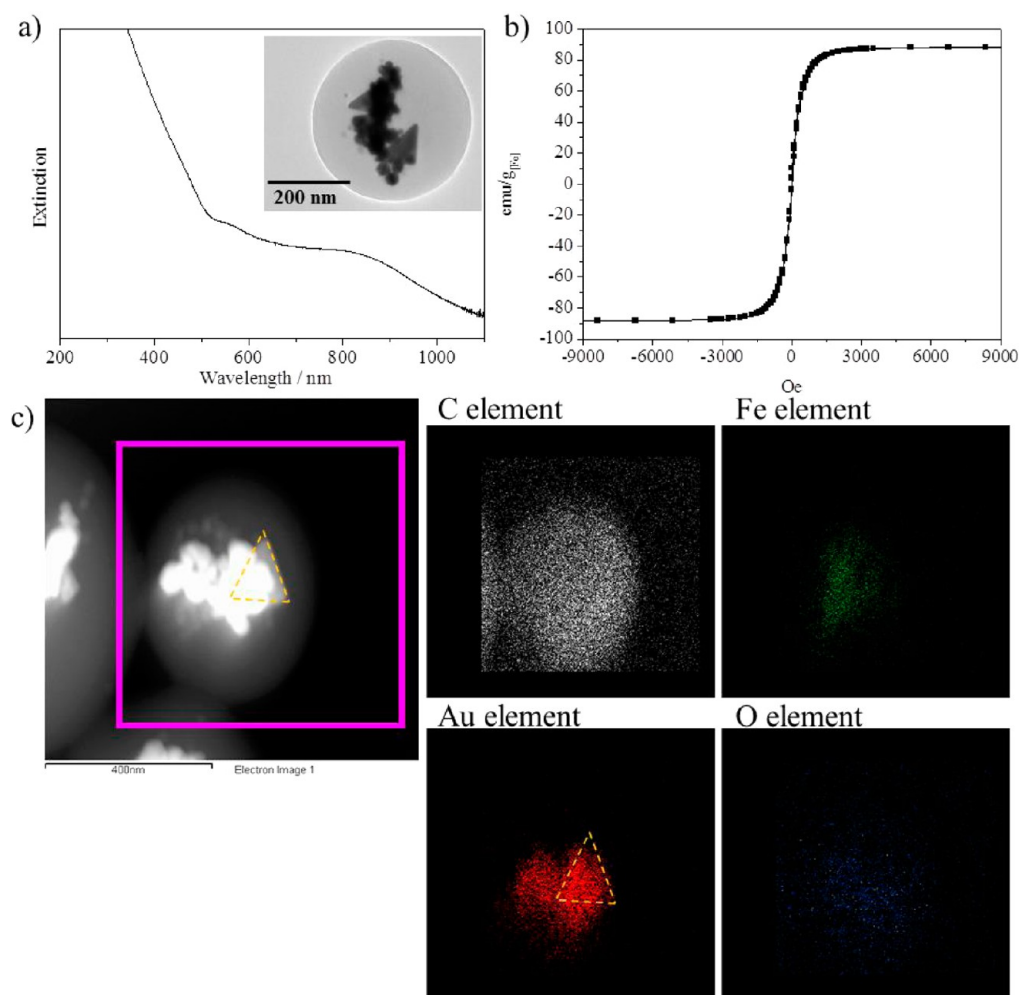


Figure 7. (a) UV–visible absorption spectrum with TEM image in the inset, (b) SQUID measurement, and (c) TEM-EDS mapping records for as-synthesized Au multicore and CTA⁺-coated Fe₃O₄ NPs@polymer structures. The yellow dashed line in c shows the triangle shape of Au nanoparticle.

Fe₃O₄ NPs obtained in the interior of the polymer particle. This synthesis reaction was carried out under the condition of including 18 μ L of HCl. These nanoproducts appeared to have NIR absorption (Figure 7a) and superparamagnetic (Figure 7b) properties. The EDS mapping examinations (Figure 7c) confirmed the colocalization of the Au and Fe elements within the polymer structure, which readily contributed to the optical and magnetic features, respectively.

4. CONCLUSIONS

Au@polymer nanocomposites with tunable isolated-to-aggregated Au cores and triangular/octahedral shapes were successfully synthesized on the basis of a one-pot reaction of HAuCl₄ and PSMA precursors under specific acid concentrations and halide ion additives, respectively. The multicore Au nanostructures presented another promising technique to adjust the SPR bands to longer wavelengths. When the Au NPs are excited at the SPR wavelengths, the local field enhancement effects can significantly increase the conversion efficiencies of the photo-to-thermal and NLO processes. We also established the use of the Au–polymer NPs with the Pt drugs tethered to the polymer structure on the surface for the combined chemo–photothermal cancer therapy, which exhibited NIR-excited emission by the Au tag for a directly

visualized drug delivery system using NLO microscopy. Importantly, the enhanced NLO contrast ability could act as an imaging tag for delivery tracking in deep tissue.

Notably, the anionic carboxylate groups on the PSMA-coated inorganic NPs would have lower nonspecific binding and toxicity to cells^{62,63} and, perhaps, for node retention⁶⁴ in the next-generation theranostic platform compared with the cationic nanocarriers. Specifically, the significant multiphoton fluorescence allowed the use of multiphoton nonlinear microscopy to track the Au@polymer NPs as they carried different chemical drugs in the human body.

■ ASSOCIATED CONTENT

Supporting Information

The Supporting Information is available free of charge on the ACS Publications website at DOI: 10.1021/acsami.5b07110.

Additional TEM images, UV–visible measurements, Pt release from the Pt-medicated Au multicore@PSMA nanocarriers, MTT assay of the A549 cells with samples and different laser power densities, and nonlinear optical images for cell alone. (PDF)

AUTHOR INFORMATION

Corresponding Author

*E-mail: c2huang@mail.ncku.edu.tw, huang.chihchia@gmail.com.

Notes

The authors declare no competing financial interest.

ACKNOWLEDGMENTS

This work was supported by the Ministry of Science and Technology, Taiwan (MOST 103-2113-M-010-001-MY2).

REFERENCES

- (1) Bogart, L. K.; Pourroy, G.; Murphy, C. J.; Puentes, V.; Pellegrino, T.; Rosenblum, D.; Peer, D.; Lévy, R. Nanoparticles for Imaging, Sensing, and Therapeutic Intervention. *ACS Nano* **2014**, *8*, 3107–3122.
- (2) Huang, C.-C.; Chang, P.-Y.; Liu, C.-L.; Xu, J.-P.; Wu, S.-P.; Kuo, W.-C. New Insight on Optical and Magnetic Fe₃O₄ Nanoclusters Promising for Near Infrared Theranostic Applications. *Nanoscale* **2015**, *7*, 12689–12697.
- (3) Zhou, Z.; Kong, B.; Yu, C.; Shi, X.; Wang, M.; Liu, W.; Sun, Y.; Zhang, Y.; Yang, H.; Yang, S. Tungsten Oxide Nanorods: An Efficient Nanoplatfor for Tumor CT Imaging and Photothermal Therapy. *Sci. Rep.* **2014**, *4* (3653), 1–10.
- (4) Zhen, Z.; Tang, W.; Chuang, Y.; Todd, T.; Zhang, W.; Lin, X.; Niu, G.; Liu, G.; Wang, L.; Pan, Z.; Chen, X.; Xie, J. Tumor Vasculature Targeted Photodynamic Therapy for Enhanced Delivery of Nanoparticles. *ACS Nano* **2014**, *8*, 6004–6013.
- (5) Chien, C. T.; Yan, J.; Chiu, W.; Wu, T.; Liu, C.; Lin, S. Caged Pt Nanoclusters Exhibiting Corrodibility to Exert Tumor-Inside Activation for Anticancer Chemotherapeutics. *Adv. Mater.* **2013**, *25*, 5067–5073.
- (6) Lee, S.; Tsai, D.; Hackley, V. A.; Brechbiel, M. W.; Cook, R. F. Surface-engineered Nanomaterials as X-ray Absorbing Adjuvant Agents for Auger-mediated Chemo-radiation. *Nanoscale* **2013**, *5*, 5252–5256.
- (7) Barry, N. P. E.; Sadler, P. J. Challenges for Metals in Medicine: How Nanotechnology May Help To Shape the Future. *ACS Nano* **2013**, *7*, 5654–5659.
- (8) Chin, C. F.; Yap, S. Q.; Li, J.; Pastorin, G.; Ang, W. H. Ratiometric Delivery of Cisplatin and Doxorubicin using Tumour-Targeting Carbon-nanotubes Entrapping Platinum(IV) Prodrugs. *Chem. Sci.* **2014**, *5*, 2265–2270.
- (9) Dai, Y.; Xiao, H.; Liu, J.; Yuan, Q.; Ma, P.; Yang, D.; Li, C.; Cheng, Z.; Hou, Z.; Yang, P.; Lin, J. In Vivo Multimodality Imaging and Cancer Therapy by Near-Infrared Light-Triggered trans-Platinum Pro-Drug-Conjugated Upconversion Nanoparticles. *J. Am. Chem. Soc.* **2013**, *135*, 18920–18929.
- (10) Hong, S.; Shuford, K. L.; Park, S. Shape Transformation of Gold Nanoplates and their Surface Plasmon Characterization: Triangular to Hexagonal Nanoplates. *Chem. Mater.* **2011**, *23*, 2011–2013.
- (11) Ye, E.; Win, K. Y.; Tan, H. R.; Lin, M.; Teng, C. P.; Mlayah, A.; Han, M. Y. Plasmonic Gold Nanocrosses with Multidirectional Excitation and Strong Photothermal Effect. *J. Am. Chem. Soc.* **2011**, *133*, 8506–8509.
- (12) Chen, J.; Glaus, C.; Laforest, R.; Zhang, Q.; Yang, M.; Gidding, M.; Welch, M. J.; Xia, Y. Gold Nanocages as Photothermal Transducers for Cancer Treatment. *Small* **2010**, *6*, 811–817.
- (13) Huang, X.; El-Sayed, I. H.; Qian, W.; El-Sayed, M. A. Cancer Cell Imaging and Photothermal Therapy in the Near-Infrared Region by Using Gold Nanorods. *J. Am. Chem. Soc.* **2006**, *128*, 2115–2120.
- (14) Tong, L.; Cogley, C. M.; Chen, J.; Xia, Y.; Cheng, J. X. Bright Three-Photon Luminescence from Gold/Silver Alloyed Nanostructures for Bioimaging with Negligible Photothermal Toxicity. *Angew. Chem., Int. Ed.* **2010**, *49*, 3485–3488.
- (15) Jang, B.; Kim, Y. S.; Choi, Y. Effects of Gold Nanorod Concentration on the Depth-Related Temperature Increase During Hyperthermic Ablation. *Small* **2011**, *7*, 265–270.
- (16) Ungureanu, C.; Kroes, R.; Petersen, W.; Groothuis, T. A. M.; Ungureanu, F.; Janssen, H.; van Leeuwen, F. W. B.; Kooyman, R. P. H.; Manohar, S.; van Leeuwen, T. G. Light Interactions with Gold Nanorods and Cells: Implications for Photothermal Nanotherapeutics. *Nano Lett.* **2011**, *11*, 1887–1894.
- (17) Sotiriou, G. A.; Starsich, F.; Dasargyri, A.; Wurnig, M. C.; Krumeich, F.; Boss, A.; Leroux, J.; Pratsinis, S. E. Photothermal Killing of Cancer Cells by the Controlled Plasmonic Coupling of Silica-Coated Au/Fe₂O₃ Nanoaggregates. *Adv. Funct. Mater.* **2014**, *24*, 2818–2827.
- (18) Hu, M.; Chen, J.; Li, Z.-Y.; Au, L.; Hartland, G. V.; Li, X.; Marquez, M.; Xia, Y. Gold Nanostructures: Engineering Their Plasmonic Properties for Biomedical Applications. *Chem. Soc. Rev.* **2006**, *35*, 1084–1094.
- (19) Jana, N.; Gearheart, L.; Murphy, C. J. Wet Chemical Synthesis of High Aspect Ratio Cylindrical Gold Nanorods. *J. Phys. Chem. B* **2001**, *105*, 4065–4067.
- (20) Hayashi, K.; Nakamura, M.; Miki, H.; Ozaki, S.; Abe, M.; Matsumoto, T.; Ishimura, K. Gold Nanoparticle Cluster–Plasmon-Enhanced Fluorescent Silica Core–Shell Nanoparticles for X-ray Computed Tomography–fluorescence Dual-Mode Imaging of Tumors. *Chem. Commun.* **2013**, *49*, 5334–5336.
- (21) Liu, H.; Liu, T.; Wu, X.; Li, L.; Tan, L.; Chen, D.; Tang, F. Targeting Gold Nanoshells on Silica Nanorattles: a Drug Cocktail to Fight Breast Tumors via a Single Irradiation with Near-Infrared Laser Light. *Adv. Mater.* **2012**, *24*, 755–761.
- (22) Kim, J.; Park, S.; Lee, J. E.; Jin, S. M.; Lee, J. H.; Lee, I. S.; Yang, I.; Kim, J. S.; Kim, S. K.; Cho, M. H.; Hyeon, T. Designed Fabrication of Multifunctional Magnetic Gold Nanoshells and Their Application to Magnetic Resonance Imaging and Photothermal Therapy. *Angew. Chem., Int. Ed.* **2006**, *45*, 7754–7758.
- (23) Cheng, L.; Yang, K.; Li, Y.; Chen, J.; Wang, C.; Shao, M.; Lee, S. T.; Liu, Z. Facile Preparation of Multifunctional Upconversion Nanoprobes for Multimodal Imaging and Dual-Targeted Photothermal Therapy. *Angew. Chem., Int. Ed.* **2011**, *50*, 7385–7390.
- (24) Kleinman, S. L.; Sharma, B.; Blaber, M. G.; Henry, A.-L.; Valley, N.; Freeman, R. G.; Natan, M. J.; Schatz, G. C.; Van Duyne, R. P. Structure Enhancement Factor Relationships in Single Gold Nanoparticles by Surface-Enhanced Raman Excitation Spectroscopy. *J. Am. Chem. Soc.* **2013**, *135*, 301–308.
- (25) Wang, Y.; Li, Y. F.; Wang, J.; Sang, Y.; Huang, C. Z. End-to-End Assembly of Gold Nanorods by Means of Oligonucleotide–Mercury(II) Molecular Recognition. *Chem. Commun.* **2010**, *46*, 1332–1334.
- (26) Chen, G.; Wang, Y.; Yang, M.; Xu, J.; Goh, S. J.; Pan, M.; Chen, H. Measuring Ensemble-Averaged Surface-Enhanced Raman Scattering in the Hotspots of Colloidal Nanoparticle Dimers and Trimers. *J. Am. Chem. Soc.* **2010**, *132*, 3644–3645.
- (27) Liu, T.; Yu, J.; Chang, C. A.; Chiou, A.; Chiang, H. K.; Chuang, Y.; Wu, C.; Hsu, C.; Chen, P.; Huang, C.-C. One-Step Shell Polymerization of Inorganic Nanoparticles and Their Applications in SERS/nonlinear Optical Imaging, Drug Delivery, and Catalysis. *Sci. Rep.* **2014**, *4* (5593), 1–10.
- (28) Yu, J.; Hsu, C.-H.; Huang, C.-C.; Chang, P.-Y. Development of Therapeutic Au-Methylene Blue Nanoparticles for Targeted Photodynamic Therapy of Cervical Cancer Cells. *ACS Appl. Mater. Interfaces* **2015**, *7*, 432–441.
- (29) Teixeira, R.; Paulo, P. M. R.; Costa, S. M. B. Gold Nanoparticles in Core–Polyelectrolyte–Shell Assemblies Promote Large Enhancements of Phthalocyanine Fluorescence. *J. Phys. Chem. C* **2015**, *119*, 21612–21619.
- (30) Urban, A. S.; Shen, X.; Wang, Y.; Large, N.; Wang, H.; Knight, M. W.; Nordlander, P.; Chen, H.; Halas, N. J. Three-Dimensional Plasmonic Nanoclusters. *Nano Lett.* **2013**, *13*, 4399–4403.
- (31) Teixeira, R.; Paulo, P. M. R.; Viana, A. S.; Costa, S. M. B. Plasmon-Enhanced Emission of a Phthalocyanine in Polyelectrolyte

Films Induced by Gold Nanoparticles. *J. Phys. Chem. C* **2011**, *115*, 24674–24680.

(32) Ladj, R.; Bitar, A.; Eissa, M. M.; Fessi, H.; Mugnier, Y.; Le Dantec, R.; Elaissari, A. Polymer Encapsulation of Inorganic Nanoparticles for Biomedical Applications. *Int. J. Pharm.* **2013**, *458*, 230–241.

(33) Ray, A.; Mukundan, A.; Xie, Z.; Karamchand, L.; Wang, X.; Kopelman, R. Highly Stable Polymer Coated Nano-Clustered Silver Plates: A Multimodal Optical Contrast Agent for Biomedical Imaging. *Nanotechnology* **2014**, *25*, 445104.

(34) Xing, S.; Feng, Y.; Tay, Y. Y.; Chen, T.; Xu, J.; Pan, M.; He, J.; Hng, H. H.; Yan, Q.; Chen, H. Reducing the Symmetry of Bimetallic Au@Ag Nanoparticles by Exploiting Eccentric Polymer Shells. *J. Am. Chem. Soc.* **2010**, *132*, 9537–9539.

(35) Sánchez-Iglesias, A.; Grzelczak, M.; Altantzis, T.; Goris, B.; Pérez-Juste, J.; Bals, S.; Van Tendeloo, G.; Donaldson, S. H., Jr.; Chmelka, B. F.; Israelachvili, J. N.; Liz-Marzán, L. M. Hydrophobic Interactions Modulate Self-Assembly of Nanoparticles. *ACS Nano* **2012**, *6*, 11059–11065.

(36) Zhou, J.; Wang, P.; Wang, C.; Goh, Y. T.; Fang, Z.; Messersmith, P. B.; Duan, H. Versatile Core–Shell Nanoparticle@Metal–Organic Framework Nanohybrids: Exploiting Mussel-Inspired Polydopamine for Tailored Structural Integration. *ACS Nano* **2015**, *9*, 6951–6960.

(37) Landfester, K.; Weiss, C. K. Encapsulation by Miniemulsion Polymerization. *Adv. Polym. Sci.* **2010**, *229*, 1–49.

(38) Liao, M.-Y.; Lai, P.-S.; Yu, H.-P.; Lin, H.-P.; Huang, C.-C. Innovative Ligand-Assisted Synthesis of NIR-Activated Iron Oxide for Cancer Theranostics. *Chem. Commun.* **2012**, *48*, 5319–5321.

(39) Liu, T.-M.; Tai, S.-P.; Chang, H.-H.; Sun, C.-K. Simultaneous Multiwavelength Generation from a Mode-Locked All-Solid-State Cr:forsterite Laser. *Opt. Lett.* **2001**, *26*, 834–836.

(40) Huang, C.-C.; Chuang, K.-Y.; Huang, C.-J.; Liu, T.-M.; Yeh, C.-S. Graphite-Shelled Si Nanoparticles and Their Au/Si Heterodimers: Preparation, Photoluminescence, and Second Harmonic Generation. *J. Phys. Chem. C* **2011**, *115*, 9952–9960.

(41) Han, F.; Guan, Z.; Tan, T. S.; Xu, Q. H. Size-Dependent Two-Photon Excitation Photoluminescence Enhancement in Coupled Noble-Metal Nanoparticles. *ACS Appl. Mater. Interfaces* **2012**, *4*, 4746–4751.

(42) Guan, Z.; Polavarapu, L.; Xu, Q. H. Enhanced Two-Photon Emission in Coupled Metal Nanoparticles Induced by Conjugated Polymers. *Langmuir* **2010**, *26*, 18020–18023.

(43) Liao, M.-Y.; Wu, C.-H.; Lai, P.-S.; Yu, J.; Lin, H.-P.; Liu, T.-M.; Huang, C.-C. Surface State Mediated NIR Two-Photon Fluorescence of Iron Oxides for Nonlinear Optical Microscopy. *Adv. Funct. Mater.* **2013**, *23*, 2044–2051.

(44) Xue, C.; Métraux, G. S.; Millstone, J. E.; Mirkin, C. A. Mechanistic Study of Photomediated Triangular Silver Nanoprism Growth. *J. Am. Chem. Soc.* **2008**, *130*, 8337–8344.

(45) Feyer, V.; Plekan, O.; Tsud, N.; Cháb, V.; Matolín, V.; Prince, K. C. Adsorption of Histidine and Histidine-Containing Peptides on Au(111). *Langmuir* **2010**, *26*, 8606–8613.

(46) Malardier-Jugroot, C.; van de Ven, T. G. M.; Whitehead, M. A. Characterization of A Novel Self-Association of an Alternating Copolymer into Nanotubes in Solution. *Mol. Simul.* **2005**, *31*, 173–178.

(47) Lazzara, T. D.; Whitehead, M. A.; van de Ven, T. G. M. Effect of Chirality on π -Stacking in Styrene and Maleimide Alternating Copolymers. *J. Phys. Chem. B* **2008**, *112*, 4892–4899.

(48) Lazzara, T. D.; Whitehead, M. A.; van de Ven, T. G. M. Linear Nano-Templates of Styrene and Maleic Anhydride Alternating Copolymers. *Eur. Polym. J.* **2009**, *45*, 1883–1890.

(49) Lai, C. T.; Hong, J. L. Role of Concentration on the Formulation of Zinc Oxide Nanorods from Poly(styrene-alt-maleic acid) Template. *J. Phys. Chem. C* **2009**, *113*, 18578–18583.

(50) Lohse, S. E.; Burrows, N. D.; Scarabelli, L.; Liz-Marzán, L. M.; Murphy, C. J. Anisotropic Noble Metal Nanocrystal Growth: The Role of Halides. *Chem. Mater.* **2014**, *26*, 34–43.

(51) Wiley, B.; Herricks, T.; Sun, Y.; Xia, Y. Polyol Synthesis of Silver Nanoparticles: Use of Chloride and Oxygen to Promote the Formation of Single-Crystal, Truncated Cubes and Tetrahedrons. *Nano Lett.* **2004**, *4*, 1733–1739.

(52) Ojea-Jiménez, I.; Romero, F. M.; Bastús, N. G.; Puntès, V. Small Gold Nanoparticles Synthesized with Sodium Citrate and Heavy Water: Insights into the Reaction Mechanism. *J. Phys. Chem. C* **2010**, *114*, 1800–1804.

(53) Enustun, B. V.; Turkevich, J. Coagulation of Colloidal Gold. *J. Am. Chem. Soc.* **1963**, *85*, 3317–3328.

(54) Hall, M. D.; Amjadi, S.; Zhang, M.; Beale, P. J.; Hambley, T. W. The Mechanism of Action of Platinum(IV) Complexes in Ovarian Cancer Cell Lines. *J. Inorg. Biochem.* **2004**, *98*, 1614–1624.

(55) Graf, N.; Lippard, S. J. Redox Activation of Metal-Based Prodrugs as a Strategy for Drug Delivery. *Adv. Drug Delivery Rev.* **2012**, *64*, 993–1004.

(56) Wilson, J. J.; Lippard, S. J. Synthesis, Characterization, and Cytotoxicity of Platinum(IV) Carbamate Complexes. *Inorg. Chem.* **2011**, *50*, 3103–3115.

(57) Matsumoto, K.; Sakai, K.; Nishio, K.; Tokisue, Y.; Ito, R.; Nishide, T.; Shichi, Y. Syntheses, Crystal Structures, and Electronic, ESR, and X-Ray Photoelectron Spectra of Acetamidate- and 2-fluoroacetamidate-bridged Mixed-Valent Octanuclear Platinum Blues. *J. Am. Chem. Soc.* **1992**, *114*, 8110–8118.

(58) Hall, M. D.; Hambley, T. W. Platinum(IV) Antitumour Compounds: Their Bioinorganic Chemistry. *Coord. Chem. Rev.* **2002**, *232*, 49–67.

(59) Pan, H.; Jiang, H.; Chen, W. The Biodegradability of Electrospun Dextran/PLGA Scaffold in a Fibroblast/Macrophage Co-culture. *Biomaterials* **2008**, *29*, 1583–1592.

(60) Santerre, J. P.; Labow, R. S.; Duguay, D. G.; Erfle, D.; Adams, G. A. Biodegradation Evaluation of Polyether and Polyester-Urethanes with Oxidative and Hydrolytic Enzymes. *J. Biomed. Mater. Res.* **1994**, *28*, 1187–1199.

(61) Zheng, M.; Zhao, P.; Luo, Z.; Gong, P.; Zheng, C.; Zhang, P.; Yue, C.; Gao, D.; Ma, Y.; Cai, L. Robust ICG Theranostic Nanoparticles for Folate Targeted Cancer Imaging and Highly Effective Photothermal Therapy. *ACS Appl. Mater. Interfaces* **2014**, *6*, 6709–6716.

(62) Wilhelm, C.; Billotey, C.; Roger, J.; Pons, J. N.; Bacri, J. C.; Gazeau, F. Intracellular Uptake of Anionic Superparamagnetic Nanoparticles as a Function of Their Surface Coating. *Biomaterials* **2003**, *24*, 1001–1011.

(63) Zhao, F.; Zhao, Y.; Liu, Y.; Chang, X.; Chen, C.; Zhao, Y. Cellular Uptake, Intracellular Trafficking, and Cytotoxicity of Nanomaterials. *Small* **2011**, *7*, 1322–1337.

(64) Rao, D. A.; Forrest, M. L.; Alani, A. W.; Kwon, G. S.; Robinson, J. R. Biodegradable PLGA Based Nanoparticles for Sustained Regional Lymphatic Drug Delivery. *J. Pharm. Sci.* **2009**, *99*, 2018–2031.